3D Printed Micro-Cells for Phase Control in 5G mmWave Applications

VITO BASILE [ID][1], **VALERIA MARROCCO** [ID][1], **MANUELA SPINA** [ID][2], **IRENE FASSI** [ID][3], **ANTONELLA D'ORAZIO** [ID][2], **(Member, IEEE), AND MARCO GRANDE** [ID][2]

[1]Institute of Intelligent Industrial Technologies and Systems for Advanced Manufacturing, National Research Council (STIIMA CNR), 70124 Bari, Italy
[2]Department of Electrical and Information Engineering DEI, Politecnico di Bari, 70125 Bari, Italy
[3]Institute of Intelligent Industrial Technologies and Systems for Advanced Manufacturing, National Research Council (STIIMA CNR), 20133 Milano, Italy

Corresponding author: Vito Basile (vito.basile@stiima.cnr.it)

ABSTRACT In this work, the design, fabrication and characterization of micro-air-channel-based unit cells aimed at phase control exploitable in 5G-mmwave applications are reported. The basic unit cell consisted of rectangular dielectric blocks (RDB) placed onto a thin substrate, realized by means of a resin polymer. The RDB effective relative permittivity was changed by tuning specific design parameters and infill density percentage (ID%), that was engineered through the introduction of a number of uniformly distributed micro-air channels. The reflected phase variation was numerically quantified in terms of frequency range and ID%, thus proving that a controlled phase variation can be accomplished depending on air-channel number. The prototypes were fabricated by means of the micro-inverted Stereolithography (SLA). In order to assess the accuracy of the SLA technology on the dimensions imposed by the high aspect ratio of the structures, larger unit cells operating in the X band were first fabricated. The acquired technological know-how has been subsequently exploited to fabricate smaller unit cells operating at mmwave. Geometrical characterizations of the prototypes, performed via a visual system setup, put in evidence the technological challenges, especially faced to realize open micro-air channels. In particular, as smaller micro-channel were actually obtained for some samples, a consequent increase of the actual ID% and effective relative permittivity values was experienced by the related unit cells. Nonetheless, the experimental results performed on the fabricated prototypes in the X band and mmwave range were in good agreement with the numerical ones, confirming the phase variation vs. ID% trends of the simulated unit cell arrays.

INDEX TERMS 5G communications, additive manufacturing, antenna arrays, antenna measurements, layered manufacturing, millimeter wave communication, reflectarray, smart surfaces, stereolithography, vision systems.

I. INTRODUCTION

Fifth-Generation (5G) communications have recently attracted the attention of the scientific community and of the wider public due to their promise to enhance and accelerate the interconnection among devices and people [1]. Nonetheless, despite its diffusion, the availability of highly efficient antennas and devices tackling the task of high data rate with negligible losses is still one of the main challenges. Additionally, similar issues are faced in the development of next-generation payloads in the mmwave and sub-THz range also aimed at space applications, which must be lightweight and multi-band, in order to guarantee the required spatial

The associate editor coordinating the review of this manuscript and approving it for publication was Antonino Orsino [ID].

resolution and sensitivity along both earth-space segments. Therefore, the design and fabrication of these systems exhibit several issues to be addressed.

When designing surfaces operating at such high frequencies, the material losses are the major concern, since they affect gain and radiation efficiency. In this scenario, reflectarray antennas (RAs), transmit arrays (TAs) and integrated lens arrays (ILAs) may have a key role when it comes to accomplishing improved performance. In particular, the use of dielectric elements and the tailoring of their dielectric properties represent an excellent solution to enhance the bandwidth, as well as an interesting alternative in the view of reducing the overall system weight. The very recent topic related to the design and fabrication of such 5G-mmwave devices focuses on the arrangements of dielectric elements

made of low relative permittivity (ε_r) materials. This scientific orientation is motivated by the following two main reasons: i. bandwidth improvement; ii. opportunity to simplify and gain flexibility in device fabrication via additive manufacturing (AM) technologies. However, in order to realize dielectric-based surfaces, the first step is the design and the optimization of the unit cell composing the whole arrangement. The design of the unit cell is a delicate task, since the elements must introduce controllable phase shift, which can be generally accomplished by a variation of the effective relative permittivity (ε_{r-eff}). Concerning RAs and TAs, the tailoring of ε_{r-eff} was generally obtained by changing one of the geometrical parameters of the element of the basic RA/TA unit cell. To this regard, the authors in [2] proposed a unit cell based on cross-shaped metamaterial slab, fabricated by Fused Deposition Modeling (FDM), placed on a metal ground; different ε_{r-eff} values were obtained by varying the gap width of the slab, and thus realizing cross-like shapes with diverse arms width. The simulation results showed that, in this way, a full 360 degrees range of phase shifts at 9.3GHz could be accomplished through a continuous variation of ε_{r-eff}, from 1.4 to 5.0. In [3], three RAs designed to operate at 100 GHz were proposed; the unit cells were made of dielectric slab elements with variable height placed on a conductor plane and fabricated via polymer jetting. The results showed that the change of ε_r (from 2.78 to 2.70) and loss tangent $\tan\delta$ (from 0.02 to 0.05) provided three different reflected phase variations, measured in the center of each device: 3.7, 187.5 and 190 degrees.

Dielectric resonator antennas (DRAs) located on a thin substrate were considered as unit cells for a RA operating in the Ka band (26-40 GHz) [4]: the relative permittivity variation and consequent phase shift were accomplished by changing the DRA length. The unit cells were fabricated by means of fused deposition modelling (FDM) and acrylonitrile butadiene styrene (ABS) material, which was properly modified to increase the original dielectric characteristics ($\varepsilon_r = 4.4$ and $\tan\delta = \sim 0.008$). Differently from previous works, a novel concept of unit cell for a TA operating at 30 GHz was proposed in [5]: the unit cell was a three-layers dielectric structure, composed by a central layer featuring a square hole with varying size sandwiched between two identical layers having tapered holes. However, as the final TA was fabricated by polymer jetting, the original designed unit cells were modified to enable their manufacturing. Measurements on prototypes were satisfactory, thus proving the feasibility of AM technologies and related dielectric materials in these applications. Graded lens, operating between 19 and 25 GHz was described in [6]–[7]: the lens was fabricated by means of Preperm ABS material and fused filament-based AM technology. In particular, the desired grading of ε_r and $\tan\delta$ was accomplished by acting on two parameters setting of the FDM machine, i.e. infill density (ID) percentage and infill pattern. Similarly, the ID percentage was also exploited as key parameter in the design and fabrication of an Integrated Lens Array (ILA) made of polylactic acid (PLA) [8]. The

lens array was realized by FDM, with the goal of reducing dielectric loss and lens weight, and speeding up the fabrication time thus decreasing cost. The authors also provided a parametric analysis on three different ID values and different deposition patterns, showing how each ID and orientation of the deposited material affected the PLA permittivity and loss tangent, and consequently, the performance of the final ILAs.

As it can be noticed, the relative permittivity of a unit cell can be modified in at least two ways: by varying the geometrical parameters of the unit cell, or the infill pattern and sizing by the exploitation of some AM technology settings, such as ID%.

In the present work, unit cells are designed and fabricated considering the combination of both approaches. The proposed basic unit cell (UC) is composed by a rectangular dielectric block (RDB) located on a thin substrate, similar to that reported in [4]. In order to provide a controllable phase variation, the relative permittivity of each RDB was changed by acting on both the RDB length and ID%. As ID% refers generally to the percentage of polymer material with respect to air, this concept can be applied to other AM technologies, different from extrusion-based processes. Therefore, as described in Section II, the ID% was implemented artificially by introducing a number of squared air micro-channels within each RDB: this action allowed to fine-tune the relative permittivity of each unit cell and, consequently, control the induced phase shift variation on a wider frequency range. Numerical results, reported in Section III and achieved via Finite Element Method (FEM) analyses, showed that UCs with different value of ID% provide controlled phase shifts over wideband frequency ranges (10-12 GHz, 26-40 GHz), depending on the air-channel number. Some prototypes, described in Section IV-A, were then fabricated by micro-inverted stereolithography (SLA). In order to assess the accuracy of the SLA technology on dimensions and tolerances imposed, especially, by the high aspect ratio of the air-channels, larger UCs operating in the X band were first fabricated. Subsequently, improvements were achieved in fabricating smaller UCs operating at mmwave. The geometrical characterization of the prototypes was performed by means of a visual system setup, which gave evidence to the impact of dimensional accuracy on the actual ID% and corresponding actual ε_{r-eff} values (Section IV-C). Finally, Scattering parameter S_{11} and phase shift measurements were performed in the X band and mmwave range on the fabricated UC arrangements: results and discussion are reported in Sections V and VI.

II. DESIGN OF THE UNIT CELL

Without loss of generality, in order to verify the impact of the ID% tuning on the phase behavior, the unit cell design will refer to a RA configuration. The periodic arrangement of a number of UCs, considering periodicities P_x and P_y along x and y axes respectively, is reported in Figure 1a. The basic unit cell (UC) is composed by a rectangular dielectric block (RDB) located at the center of a grounded thin
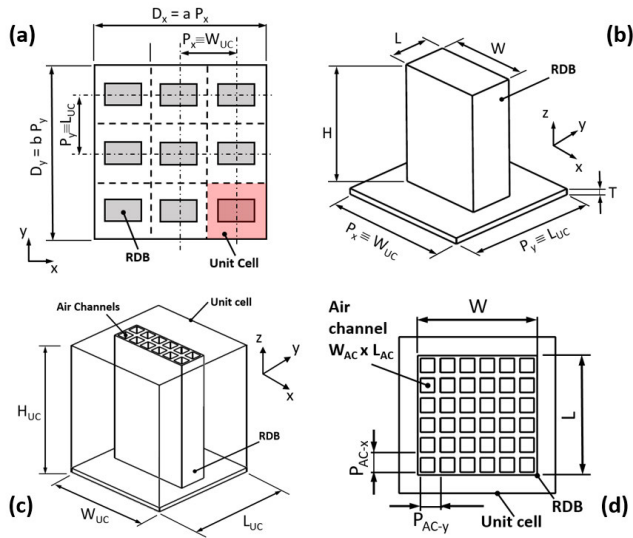
FIGURE 1. a) Periodic arrangement of unit cells; b) Full bulk RDB-based UC; c) UC composed by RDB and 6 × 2 air channels; d) UC with air 6 × 6 channels arrangement within the RDB, considering $P_{ACx} = P_{ACy} = 0.7$ mm along x and y axes.

dielectric layer (Figure 1b-c); the RDB can be a full bulk structure (Figure 1b) or a micro-structured one (Figure 1c), featuring periodically arranged channels (Figure 1d). The squared air channels have section equal to 0.5 mm × 0.5 mm each and are periodically arranged considering constant pitch along both x-y axes equal to $P_{ACx} = P_{ACy} = 0.7$ mm (Figure 1d).

With the introduction of the air channels, the polymer volume of the RDB is reduced, and consequently the ε_{r-eff} can be controllably decreased varying the infill density (ID%) explicated by equation (1):

$$ID\% = \frac{V_{RDB} - n \cdot m \cdot V_{AC}}{V_{UC}} \cdot 100 \quad (1)$$

where V_{RDB} is the volume of the bulk polymeric structure without air channels, V_{AC} is the volume of a single air channel introduced within the RDB, "n" and "m" are the numbers of air channels along x and y axes, respectively and V_{UC} is the volume of the overall unit cell. Bulk RDBs have different ID% in relation to their dimensions: for instance, by keeping height H and width W fixed, if the RDB length L is equal to 4.2 mm, the ID% is 69.93%, while for a length L equal to 1.4 mm, the ID% is 25.36%. The ID% would be 100% only in case of RDB coincident with the whole unit cell area (Figure 1c), i.e. the ε_{r-eff} would correspond to the actual one of the finite dielectric blocks.

Table 1 shows the main design parameters of UC and RDB and periodicities of the Unit Cell and air channels. It is worth noticing that the overall UC array dimensions, indicated by D_x and D_y, were adjusted to fit the WR90 and WR28 waveguide sections (22.86 mm × 10.16 mm and 7.11 mm × 3.55 mm, respectively).

Table 2 shows twenty configurations achievable with the indicated sizes. In particular, the first twelve configurations are fabricated for WR90 measurements and feature air

TABLE 1. Nominal dimensional parameter of the UC, RDB and periodic arrangement.

Symbol	Definition	Value [mm] X Band WR90	Value [mm] mmwave WR28
W	RDB width	4.2	2.8
L	RDB length	1.4, 4.2	1.4, 2.8
H	RDB height	6.3	
T	RDB Substrate thickness	0.2	
W_{UC}	Unit Cell width	5.5	3.5
L_{UC}	Unit Cell length	4.65	3.5
H_{UC}	Unit Cell height (H_{UC}=H+T)	6.5	
P_x	x-Periodicity (P_x=W_{UC})	5.5	3.5
P_y	y-Periodicity (P_y=L_{UC})	4.65	3.5
a	Number of Unit Cells along the x-axis	4	2
b	Number of Unit Cells along the y-axis	2	1
D_x	Total length of the periodic array (D_x=a·P_x)	22	7
D_y	Total width of the periodic array (D_y=b·P_y)	9.3	3.5
n	Number of air channels along x-direction	0, 6	0, 4
m	Number of air channels along y-direction	0, 1, ..., 6	0, 1, ..., 4
W_{AC}	Air Channel width	0.5	
L_{AC}	Air Channel length	0.5	
P_{ACx}, P_{ACy}	Air Channels xy-periodicity (P_{ACx}= P_{ACy})	0.7	

TABLE 2. Infill density resolution, unit cell dimensions and air channels distribution.

UC	Width W [mm]	Length L [mm]	Height H+T [mm]	Volume V_{RDB} [mm³]	Width W_{AC} [mm]	Length L_{AC} [mm]	Height H_{AC} [mm]	Layout n x m [-]	# AC nm [-]	Volume nm V_{AC} [mm³]	Infill Density ID [%]	Resolution IDR [%]
61B	4,20	0,70		23,64						0,00	14,22%	
62B	4,20	1,40		42,16						0,00	25,36%	
63B	4,20	2,10	6,50	60,68						0,00	36,50%	9,42%
64B	4,20	2,80		79,20						0,00	47,64%	
65B	4,20	3,50		97,73						0,00	58,79%	
66B	4,20	4,20		116,25						0,00	69,93%	
61C	4,20	0,70		23,64	0,500	0,500	6,500	1x6	6	9,75	8,35%	
62C	4,20	1,40		42,16	0,500	0,500	6,500	2x6	12	19,50	13,63%	
63C	4,20	2,10	6,50	60,68	0,500	0,500	6,500	3x6	18	29,25	18,91%	4,46%
64C	4,20	2,80		79,20	0,500	0,500	6,500	4x6	24	39,00	24,18%	
65C	4,20	3,50		97,73	0,500	0,500	6,500	5x6	30	48,75	29,46%	
66C	4,20	4,20		116,25	0,500	0,500	6,500	6x6	36	58,50	34,74%	
41B	2,80	0,70		14,80						0,00	18,58%	
42B	2,80	1,40	6,50	27,15						0,00	34,09%	15,51%
43B	2,80	2,10		39,49						0,00	49,60%	
44B	2,80	2,80		51,84						0,00	65,11%	
41C	2,80	0,70		14,80	0,500	0,500	6,500	1x4	4	6,50	10,42%	
42C	2,80	1,40		27,15	0,500	0,500	6,500	2x4	8	13,00	17,77%	7,34%
43C	2,80	2,10	6,50	39,49	0,500	0,500	6,500	3x4	12	19,50	25,11%	
44C	2,80	2,80		51,84	0,500	0,500	6,500	4x4	16	26,00	32,45%	

channels sizes equal to 0.5 mm × 0.5 mm × 6.5 mm; UC 5.5 mm × 4.65 mm × 6.5 mm, substrate thickness of 0.2 mm, RDB sizes 4.2 mm × 4.2 mm × 6.3 mm. The last smaller eight configurations are devoted to WR28 measurements and exhibit air channels sizes 0.5 mm × 0.5 mm × 6.5 mm; UC 3.5 mm × 3.5 mm × 6.5 mm, substrate thickness of 0.2 mm, RDB sizes 3.5 mm × 3.5 mm × 6.3 mm. The configurations 1-6 are the bulk RDB-based (from 61B to 66B) which provide an ID% ranging between 14.22-69.93%. In this case, the resolution of the engineered ID% values is equal to 9.42%. Conversely, configurations 7-12 relate to RDB with air channels (from 61C to 66C), which allow to have ID% values ranging between 8.35-34.74%, with a resolution of 4.46%, thus proving that the presence of the micro-air channels enables a more accurate control over the ε_{r-eff}. The bulk RDB-based configurations 13-16 (from 41B to 44B) assess an ID% between 18.58-65.11%; in this case, the resolution
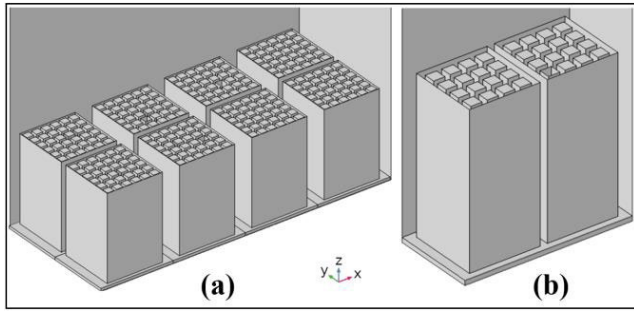
FIGURE 2. Array of UCs. (a) Array of 4 × 2 UCs corresponding to configuration 66C in a WR90 and (b) Array of 2 × 1 UCs corresponding to configuration 44C in a WR28; the air channels are here represented as smaller blocks within the RDB.

related to the engineered ID% values is equal to 15.51%. The configurations 17-20 refer to RDB with air channels (from 41C to 44C) and provide ID% values ranging between 10.42-32.45%, with an engineered ID resolution equal to 7.34%.

III. REFLECTED PHASE ASSESSMENT

In order to quantify the reflected phase of the UCs in the frequency range of interest, between 10-40 GHz, numerical analyses were performed on arrays of UCs by means of Finite Element Method implemented via the COMSOL Multiphysics software [9]. The electromagnetic approach chosen for the analysis was based on One-Port cell configuration involving Perfect Electric Conductors (PEC) to simulate both rectangular waveguides, WR90 and WR28, and the ground plane supporting the UCs. Perfect Matched Layer (PML) were used along the z-axis in order to avoid unwanted reflections. Both WR90 and WR28 were only excited by means of the fundamental mode TE_{10} in the ranges equal to 10-12 GHz and 20-40 GHz, respectively, in order to avoid multimode propagation. In particular, the numerical calculations were performed on arrangements of UCs corresponding to 62B and 62C, 66B and 66C, 42B and 42C, 44B and 44C configurations (Table 2, Figure 2); the air-channels are represented as smaller blocks within the RDB.

The arrays composed by the bigger UCs were inserted into a WR90 while, for the mmwave range (20-40 GHz) analysis, the smaller arrays of UCs, involving 42B, 42C, 44B and 44C RDBs, were considered. The numerical results related to the reflected phase of the UCs in function of the frequency range pertaining WR90 (10 – 12 GHz) and WR28 (20 – 40 GHz) analyses are plotted in Figure 3.

As clearly visible from Figure 3a, referring to the UCs inserted in the WR90 waveguide, the reflected phases measured for all samples follow a linear behavior and the phase variation detected between same bulk and channeled configurations is kept constant throughout the X band. In particular, the phase variation $\Delta\Phi$ experienced by the 66B-66C configurations is equal to 63 degrees, corresponding to 1.75 deg/air-channel, while $\Delta\Phi$ is equal to 8 degrees for 62B-62C configurations, i.e. 0.67 deg/air-channel. Therefore, it is
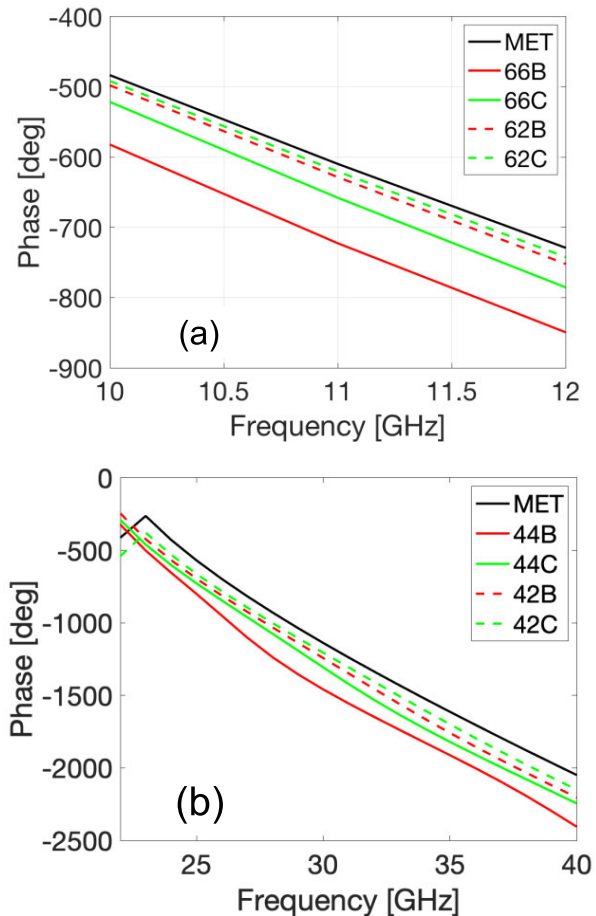

FIGURE 3. Phase distribution vs. frequency for configurations: (a) 62B (ID = 25.36%), 62C (ID = 13.63%), 66B (ID = 69.93%), 66C (ID = 34.74%) and (b) 42B (ID = 34.09 %), 42C (ID = 17.77 %), 44B (ID = 65.11 %), 44C (ID = 32.45 %).

evident that a higher ID% variation between bulk and channeled UCs leads to higher $\Delta\Phi$, obtained in a more controllable fashion. Additionally, it can be noticed that as the number of air-channels in the UC arrangement is increased, the reflected phase values become higher (solid and dashed green lines in Figure 3a) and the phase variation is about 36.80 deg/ 24 air-channel.

Numerical results concerning the smaller UCs matching WR28 waveguide sizes are reported Figure 3b. As inferable from the curves, also in this range, the reflected phases have linear trends and the phase variation detected between same bulk and channeled configurations is kept constant throughout the mmwave range band. In particular, the phase variation measured considering 44B-44C configurations (solid red and green lines) is about 121 degrees, corresponding to 7.56 deg/air-channel, while this value is about 46 degrees for 42B-42C configuration, thus obtaining 5.75 deg/air-channel. Therefore, also in this case, a higher ID% variation between bulk and channeled UCs leads to higher phase variation. Finally, referring to solid and dashed green lines in Figure 3b, the comparison between 44C-42C configurations shows that an average phase variation of about 99 deg/8 air-channels can be obtained throughout the mmwave range. Finally, it is
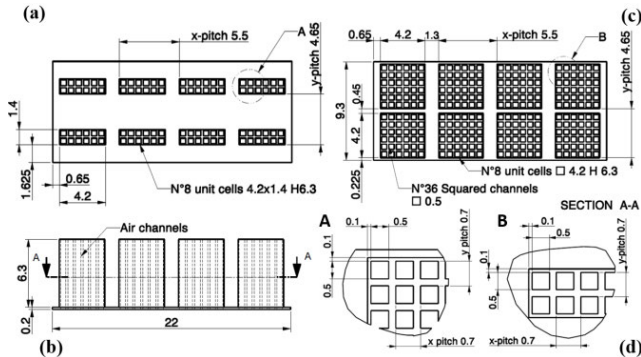
FIGURE 4. Drawings of the UC arrangements with air channels. Top view of sample 62C (a) and 66C (c); Side view of samples 66C and 62C (b); detailed views of air channels (d).

worth pointing out that, for both ranges, a similar behavior has been observed when plane wave excitation was applied to the simulations.

IV. 3D PRINTING OF THE UNIT CELL ARRAYS AND GEOMETRICAL CHARACTERIZATION OF THE PROTOTYPES

AM technologies provide rapid prototyping with significant reduction of machining time and costs and they have already proved their effectiveness at enabling the fabrication of dielectric resonator antennas (DRAs) with intriguing 3D geometries for 5G applications [10]–[12]. These technologies are very advantageous to create small form factors and complex structures, especially compared to the conventional subtractive manufacturing techniques. In this study, the main fabrication challenges were due to the overall sizes of the RDB and to the micro-scale of the air channels featuring very high aspect ratio. To address these issues, the unit cell samples were fabricated using inverted (bottom-up) Stereolithography (SLA) [13], which is capable of ensuring high-accuracy, high-resolution and good surface finishing.

A. UNIT CELL ARRAY FABRICATION VIA MICRO-INVERTED STEREOLITHOGRAPHY

Bulk UC arrays and RDB with air channels inclusion UC arrays were 3D-printed; in particular, configurations 62B, 62C, 66B, 66C, 42B, 42C, 44B and 44C (see Table 2) were fabricated. The final design was developed by means of Solidworks 3D CAD software: as an example, drawings of all prototypes are represented in figures 4 and 5. The 3D models of 66C, 62C, 44C and 42C UCs are reported in figure 6. The fabrication of all samples was made exploiting the Formlabs Form3 SLA machine (figure 7a), which provides a minimum resolution of $85 \mu m$ (laser spot diameter) and a positioning resolution of 25 μm on the XY plane. The polymerization, implying the change of state from liquid mixtures to solid, was triggered by a class 1 violet laser operating at a wavelength of 405 nm, considering a power of 250 mW. The photopolymer used for the UC arrangements fabrication was the Formlabs Tough V05 [11], [12], [14].
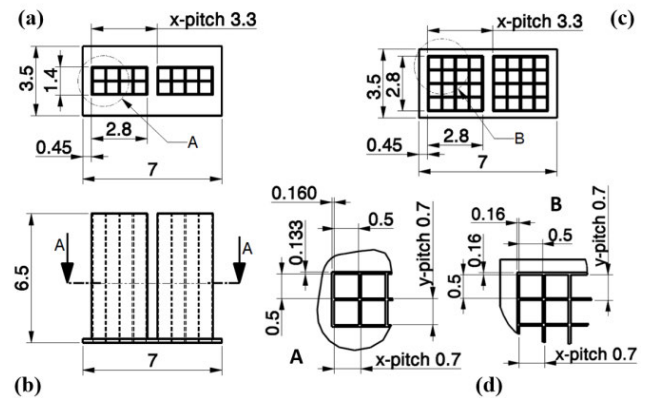

FIGURE 5. Drawings of the UC arrangements with air channels. Top view of sample 42C (a) and 44C (c); Side view of samples 42C and 44C (b); detailed views of air channels (d).
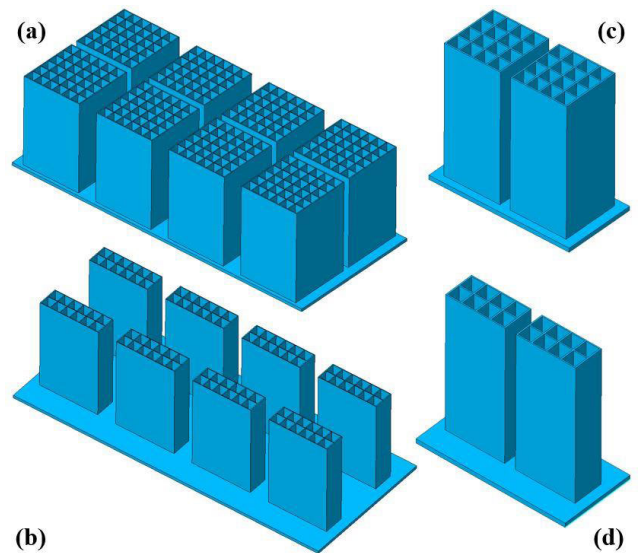

FIGURE 6. 3D solid models of UC arrays. a) Sample 66C; b) Sample 62C; c) Sample 44C; d) Sample 42C.
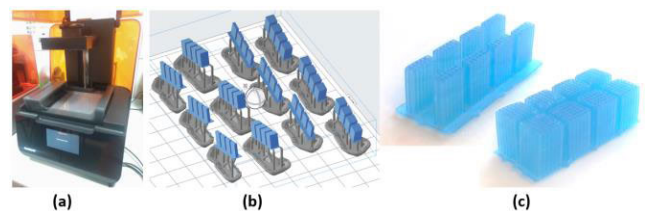

FIGURE 7. Picture of the fabrication process of UCs arrangement by means of SLA. a) Formlabs Form3 3D printer; b) Sample models pre-processing with Formlabs PreForm; c) Samples after IPA washing and UV curing.

In order to pursue higher quality of the prototypes, the layer thickness (Z-axis resolution) was set equal to 50 μm, which is the lowest value allowed by the material. For each layer, the laser spot polymerized the slice of the model according to the path generated with the software Formlabs PreForm v.3.4.2, by pre-processing the STL file of the 3D model (figure 7b).

In the specific case, the most challenging part was the realization of the micro-squared air channels, due to the cumbersome evacuation of the liquid resin out of the channels. Therefore, a proper 3D placement (orientation) of the part within the build volume was accurately selected. The channels should be aligned along the vertical z-axis of the printer as much as possible, with open sides at the bottom, in order to exploit gravity for resin evacuation. Additionally, the supports were designed to avoid interference with the flow out of the resin from the channels. After the 3D printing, the samples underwent three post-processing steps: washing, manual supports removal and additional UV curing. The washing was required to remove the residual liquid resin on the printed sample surface and also aiding the removal of the liquid resin potentially left into the air channels. To this purpose, a first washing was made via immersion of the samples into high purity 99.9% isopropyl alcohol (IPA) for 20 minutes into a Formlabs Wash machine. Washed samples are showed in figure 7c. After the immersion in IPA, an additional washing operation was performed by means of syringes and shaped funnels, preliminarily prototyped on purpose via Form3 3Dprinter. Using these customized washing tools, it was possible to force the high-purity IPA through the air channels at pressure, thus promoting the removal of residual liquid resin. A 4 bar compressed air jet was also used to push the liquid resin and IPA outside the channels. After washing and blowing, all supports were then gently removed with a cutter and, finally, the samples were exposed to UV light into a Formlabs Cure machine for 60 minutes at a temperature of 60°C for additional curing. The additional UV post-processing was aimed at improving the mechanical strength and homogeneity of the part, paying close attention, though, to avoid the polymerization of residual liquid resin into the narrow channels. The fabrication of a prototype required about 12.5 processing hours and 3 hours of post-processing operations.

B. GEOMETRICAL CHARACTERIZATION OF THE PROTOTYPES BY MEANS OF A VISUAL SYSTEM SETUP

The final prototypes were measured by using a vision system and image processing techniques, which has already been successfully exploited in other similar applications [15], [16], based on a USB digital microscope (Texon U500x) with 500x maximum magnification and resolution of 640 × 680 pixels (0.3 Mpixels). A flexible jointed arm was used to keep the microscope in the correct position, with its longitudinal axis orthogonal to the measurement plane, and at a constant distance from the surface of the samples. Four different configurations of the visual setup were defined for the RDB measurements: #1 and #3 featuring a large field-of-view (FoV) but lower magnification, and #2 and #4 exhibiting higher magnification but lower FoV, suitable for narrow micro-channels measurements (table 3). In the first and third configurations, the FoV was set to acquire and measure both sides of the RDBs, i.e. larger than squared areas □4.2 mm and □2.8 mm, while in the second and forth

TABLE 3. Parameters of the four vision systems configurations.

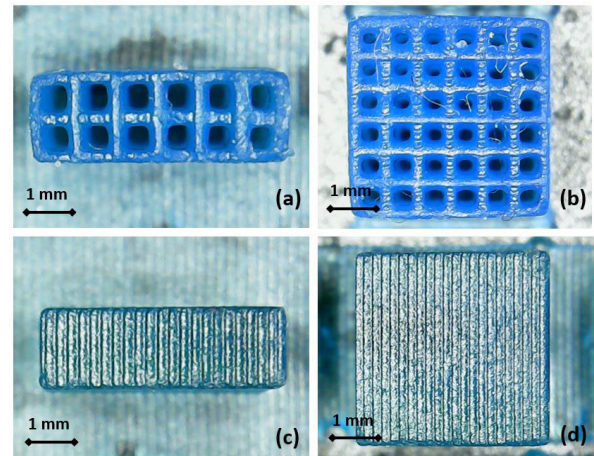| #	Scale	Image FoV				Spatial Resolution	Feature Resolution
		Width		Height		R_s	R_f
	[px/mm]	[px]	[mm]	[px]	[mm]	[μm/px]	[μm]
1	98.503	640	6.50	480	4.87	10.15	30.46
2	223.846	640	2.86	480	2.14	4.47	13.40
3	117.333	640	5.45	480	4.09	8.52	25.57
4	279.417	640	2.29	480	1.72	3.58	10.74

FIGURE 8. Images acquired with the first vision system configuration. a) RDB 4.2 × 1.4 mm ID = 13.63%; b) RDB 4.2 × 4.2 mm ID = 34.74%; c) Bulk RDB 4.2 × 1.4 mm ID = 25.36%; d) Bulk RDB 4.2 × 4.2 mm ID = 69.93%.

configurations, the magnification was maximized to effectively measure the air channels' dimensions The image scales were measured by means of a microscope micrometer calibration ruler and with the software ImageJ v.1.52a developed by the National Institute of Health NIH, USA [17]. All parameters related to the four configurations are summarized in table 3. Figures 8 and 9 show the images of samples acquired by means of the first and third visual system configurations respectively.

From visual inspection, it can be noticed that debris and burrs can be present on the samples (figures 8 and 9 a-b) while the typical layer-by-layer texture due to the fabrication process is clearly visible on the surface of the bulk samples (figures 8 and 9, c-d). Length (L) and width (W) of twenty-two samples of RDBs were measured: mean values, standard deviation (SD) and deviation of measurements from the nominal values were calculated after three measurements of each dimension. Figure 10 shows two prototypes located on the metal shorting plates of the WR90 waveguide (figure 10, a) and WR28 waveguide (figure 10, b) used for the experimental measurements.

Measurements deviate from nominal values of a quantity ranging between 34 and 271 μm. Mean standard deviations (SD) are comprised in the range of 0-86 μm. These values of SD can be also considered as an estimate of the inverted SLA machine repeatability. All measurements are summarized in table 4 and 5.
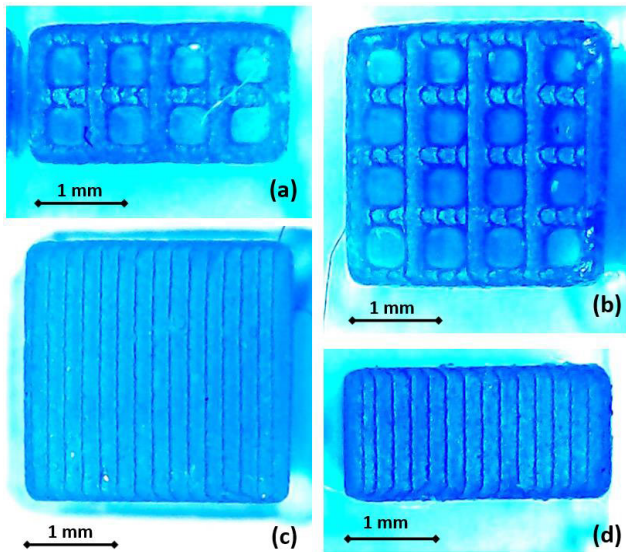
FIGURE 9. Images acquired with the third vision system configuration.
a) RDB 2.8 × 1.4 mm ID = 17.77%; b) RDB 2.8 × 2.8 mm ID = 32.45%;
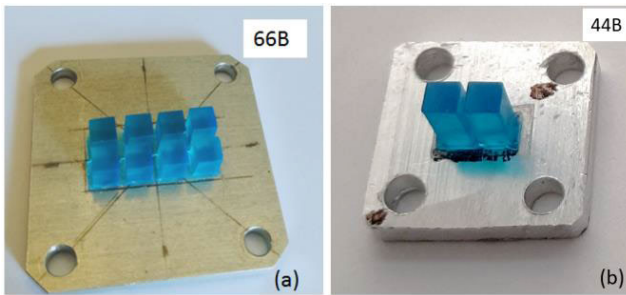c) Bulk RDB 2.8 × 2.8 mm ID = 65.11%; d) Bulk RDB 2.8 × 1.4 mm ID = 34.09%.

FIGURE 10. Samples placed at the center of shorting plates for the assembly with the waveguides. a) Sample 66B on the steel plate for WR90 waveguide; b) Sample 44B on the aluminum plate for WR28 waveguide.

TABLE 4. UC Samples measurements performed by using visual system configuration 1.

UC Prototype	Sample	Dimension	Nominal value [mm]	Mean value [mm]	Standard Deviation [mm]	Mean Deviation [mm]	Normalized Mean Deviation [%]
62B (4.2x1.4x6.5 mm; Bulk; ID=25.36%)	1	L	1.4	1.441	0.016	0.041	2.9
		W	4.2	4.288	0.056	0.088	2.1
	2	L	1.4	1.434	0.016	0.034	2.4
		W	4.2	4.274	0.031	0.074	1.8
66B (4.2x4.2x6.5 mm; Bulk; ID=69.93%)	1	L	4.2	4.261	0.041	0.061	1.5
		W	4.2	4.290	0.061	0.090	2.1
	2	L	4.2	4.255	0.039	0.055	1.3
		W	4.2	4.270	0.030	0.070	1.7
62C (4.2x1.4x6.5 mm; Air Channels; ID=13.63%)	1	L	1.4	1.544	0.027	0.144	10.3
		W	4.2	4.384	0.033	0.184	4.4
	2	L	1.4	1.539	0.027	0.139	9.9
		W	4.2	4.295	0.050	0.095	2.3
	3	L	1.4	1.598	0.037	0.198	14.1
		W	4.2	4.437	0.069	0.237	5.6
	4	L	1.4	1.559	0.040	0.159	11.4
		W	4.2	4.398	0.035	0.198	4.7
66C (4.2x4.2x6.5mm; Air Channels; ID=34.74%)	1	L	4.2	4.400	0.039	0.200	4.8
		W	4.2	4.385	0.048	0.185	4.4
	2	L	4.2	4.386	0.043	0.186	4.4
		W	4.2	4.414	0.038	0.214	5.1

TABLE 5. UC Samples measurements performed by using visual system configuration 3.

UC Prototype	Sample	Dimension	Nominal value [mm]	Mean value [mm]	Standard Deviation [mm]	Mean Deviation [mm]	Normalized Mean Deviation [%]
42B (2.8x1.4x6.5 Bulk; ID%=34.09)	1	L	2.8	2.972	0.013	0.172	6.13
		W	1.4	1.551	0.015	0.151	10.80
	2	L	2.8	2.977	0.010	0.177	6.33
		W	1.4	1.509	0.009	0.109	7.75
	3	L	2.8	3.014	0.020	0.214	7.65
		W	1.4	1.520	0.010	0.120	8.56
44B (2.8x2.8x6.5 Bulk; ID%=65.11)	1	L	2.8	2.957	0.017	0.157	5.62
		W	2.8	2.966	0	0.166	5.93
	2	L	2.8	3.060	0.009	0.260	9.27
		W	2.8	2.966	0.017	0.166	5.93
	3	L	2.8	2.966	0.037	0.166	5.93
		W	2.8	2.963	0.010	0.163	5.82
42C (2.8x1.4x6.5 Channels; ID%=17.77)	1	L	2.8	3.003	0.021	0.203	7.24
		W	1.4	1.545	0.018	0.145	10.39
	2	L	2.8	3.028	0.027	0.228	8.16
		W	1.4	1.594	0.009	0.194	13.84
	3	L	2.8	3.077	0.017	0.277	9.88
		W	1.4	1.614	0.020	0.214	15.26
44C (2.8x2.8x6.5 Channels; ID%=32.45)	1	L	2.8	3.074	0.086	0.274	9.78
		W	2.8	3.048	0.018	0.248	8.87
	2	L	2.8	3.026	0.026	0.226	8.06
		W	2.8	3.034	0.037	0.234	8.36
	3	L	2.8	3.068	0.034	0.268	9.58
		W	2.8	3.071	0.013	0.271	9.68

The second and forth vision system configurations were exploited to measure air channel sections within the UCs. The original 24-bit RGB color images (figure 11a) were also filtered with ImageJ SW via a Hue Saturation and Brightness (HSB) to highlight air channels edges (red color) (figure 11b). In particular, ten measurements for each side (width W_{AC} and length L_{AC}) were performed: mean values, SD and mean deviations from nominal values related to each air channel side are reported in table 6. The results reveal that the actual air channel sides are in the range of 316-509 μm, thus, some samples exhibit smaller air-channel sizes than the nominal ones (0.5 mm).

Measurements reported in tables 4 and 5 are also plotted in two graphs (figure 12). The dashed lines highlight the nominal dimension values, which were 1.4, 2.8, 4.2 for RDB (figure 12a) and 0.5 mm for air channels sides (figure 12b), respectively. As shown in figure 12a, being the standard deviation lower, UCs' prototypes are slightly bigger than nominal ones. Therefore, these results allow to conclude that the fabrication accuracy is about $\pm 100 \mu$m and hence in line with the 3D printing process capability.

On the contrary, figure 12b shows that the fabrication accuracy for the air channels related to UC samples meant for WR90 measurements is lower, as their actual dimensions are smaller than nominal ones. A possible explanation can be found in the residual liquid resin still remained trapped into the narrow channels and attached to the internal walls, which likely caused also rounded edges of air channels (figure 11). Conversely, smaller prototypes fabricated for WR28 waveguide (42B, 44B, 42C, 44C) exhibit air channels affected by lower deviation from nominal value due to a more effective IPA washing of channels performed with customized funnels. In addition, it can be noticed that a different fabrication

TABLE 6. Air channels sample measurements by exploiting the visual system configurations 2 and 4.

| UC Prototype	Sample	Dimension	Nominal value [mm]	Mean value [mm]	Standard Deviation [mm]	Mean Deviation [mm]	Normalized Mean Deviation [%]
62C (4.2x1.4x6.5 Channels; ID%=13.63)	1	W_AC	0.5	0.388	0.015	-0.112	-22.4
		L_AC	0.5	0.425	0.024	-0.075	-15.0
	2	W_AC	0.5	0.382	0.018	-0.118	-23.6
		L_AC	0.5	0.446	0.030	-0.054	-10.8
	3	W_AC	0.5	0.334	0.026	-0.166	-33.2
		L_AC	0.5	0.389	0.039	-0.113	-22.6
	4	W_AC	0.5	0.316	0.016	-0.184	-36.8
		L_AC	0.5	0.374	0.009	-0.126	-25.2
66C (4.2x4.2x6.5 Channels; ID%=34.74)	1	W_AC	0.5	0.354	0.012	-0.146	-29.2
		L_AC	0.5	0.424	0.012	-0.076	-15.2
	2	W_AC	0.5	0.357	0.014	-0.143	-28.6
		L_AC	0.5	0.414	0.011	-0.086	-17.2
42C (2.8x1.4x6.5 Channels; ID%=17.77)	1	W_AC	0.5	0.493	0.013	-0.007	-1.46
		L_AC	0.5	0.452	0.002	-0.048	-9.57
	2	W_AC	0.5	0.470	0.009	-0.030	-5.99
		L_AC	0.5	0.486	0.022	-0.014	-2.89
	3	W_AC	0.5	0.488	0.008	-0.012	-2.42
		L_AC	0.5	0.456	0.015	-0.044	-8.86
44C (2.8x2.8x6.5 Channels; ID%=32.45)	1	W_AC	0.5	0.499	0.002	-0.001	-0.27
		L_AC	0.5	0.488	0.002	-0.012	-2.42
	2	W_AC	0.5	0.502	0.025	0.002	0.45
		L_AC	0.5	0.509	0.005	0.009	1.88
	3	W_AC	0.5	0.451	0.016	-0.049	-9.81
		L_AC	0.5	0.472	0.009	-0.028	-5.52
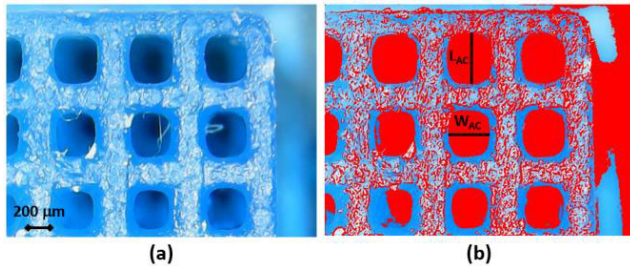
FIGURE 11. Images acquired with the vision system configuration 2. a) Raw image of air channels on the UC; b) Color threshold image processed by ImageJ with measurements of air channels width W_{AC} and length L_{AC}.

FIGURE 12. a) Mean values and standard deviations of RDB measurements of dimensions L and W; b) Mean values and standard deviations of air channels measurements of dimensions L_{AC} and W_{AC}.

FIGURE 13. Prototypes cross-section along air channels direction.

accuracy is also detected in the two direction (X-Y) due to the machine accuracy along the two axes and to the orientation of the samples into the build volume.

As inferable from visual acquisitions and measurements, from the fabrication viewpoint, the most critical issue was the liquid resin flow-out from the narrow channels. Resin high viscosity, along with surface tension and small air channel sizes resulted in difficult evacuation of the liquid photopolymer resin.

However, despite this fabrication complexity, the realization of passing air-channels within the prototypes was successful, as no obstruction can be clearly observed from the inspection of the unit cell cross section along the air channel direction, obtained by sectioning a UC sample (Figure 13). The different sizes measured for the fabricated UCs and air channels sizes lead obviously to different actual ID% compared to nominal values.

To this aim, by assuming mean values of RDB and air channel dimensions as reference, the actual ID% values can be calculated (table 7): as expected, actual ID% values increase in particular for prototypes 66C and 62C featuring air
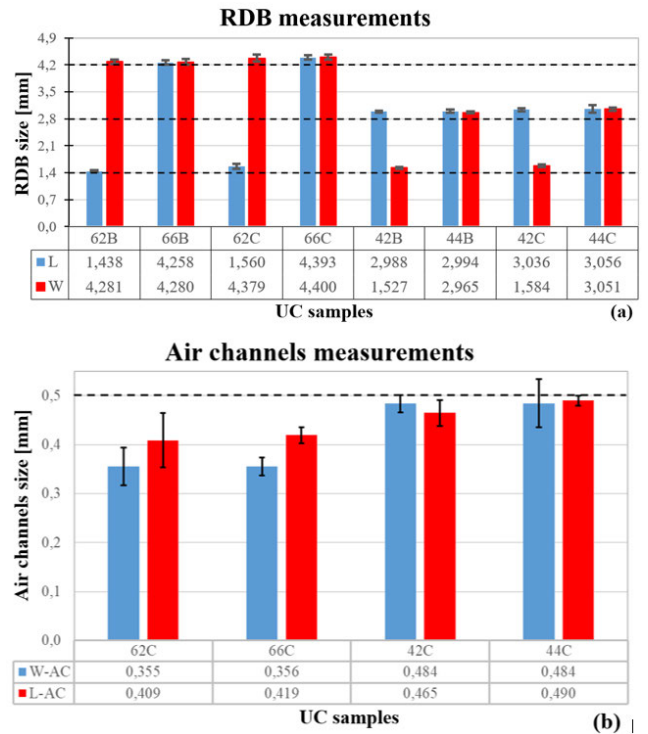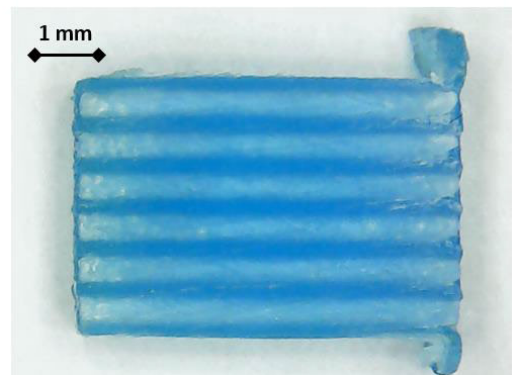
channels, as their sections were smaller than those set by the design.

C. ACTUAL RELATIVE PERMITTIVITY OF THE FABRICATED UNIT CELL

Starting from the ID%, the relative permittivity of the fabricated UCs can be retrieved. In order to obtain such data, the general rule of mixtures theory [18] can be exploited. This rule considers the empirical correlation between some physical properties and the chemical composition of materials. Indeed, it was successfully applied to composite materials [19], [20] made of a matrix and a filler or reinforcement, to predict the overall value of a mechanical properties, such as

TABLE 7. Actual ID% Estimated by means of uc and air channel measurements and comparison with nominal values.

UC	RDB				AIR CHANNELS (AC)				INFILL DENSITY	
	Width	Length	Height	Volume	Width	Length	Height	AC Volume	Nominal	Actual
	W	L	H+T	V_{RDB}	W_{AC}	L_{AC}	H_{AC}	nmV_{AC}	ID	
	[mm]	[mm]	[mm]	[mm³]	[mm]	[mm]	[mm]	[mm³]	[%]	
62B	4.34	1.52	6.50	47.53				0.00	25.36%	28.03%
66B	4.34	4.34	6.50	124.44				0.00	69.93%	74.29%
62C	4.34	1.52	6.50	47.53	0,355	0.407	6.500	11.27	13.63%	21.25%
66C	4.34	4.34	6.50	124.44	0,355	0.407	6.500	33.81	34.74%	53.96%
42B	3.02	1.55	6.50	31.89				0.00	34.09%	40.05%
44B	3.02	3.02	6.50	59.72				0.00	65.11%	75.00%
42C	3.02	1.55	6.50	31.89	0.480	0.485	6.5	12.11	17.77%	24.85%
44C	3.02	3.02	6.50	59.72	0.480	0.485	6.5	24.21	32.45%	44.59%

TABLE 8. Estimates of effective permittivity of UC SR-EFF, Calculated by equation (3).

UC	Relative Permittivity estimation				
	Relative Permittivity of Resin	Nominal		Actual	
		Infill Density	Effective Relative Permittivity	Infill Density	Effective Relative Permittivity
	ε_{Res}	$ID_N\%$	$\varepsilon_{R\text{-}Eff}^N$	$ID_A\%$	$\varepsilon_{R\text{-}Eff}^A$
62B	2.7	25.36	**1.43**	28.03	**1.48**
66B	2.7	69.93	**2.19**	74.29	**2.26**
62C	2.7	13.63	**1.23**	21.25	**1.36**
66C	2.7	34.74	**1.59**	53.96	**1.92**
42B	2.7	34.09	**1.58**	40.05	**1.68**
44B	2.7	65.11	**2.11**	75.00	**2.27**
42C	2.7	17.77	**1.30**	24.85	**1.42**
44C	2.7	32.45	**1.55**	44.59	**1.76**

Young's Modulus E, or other physical property (i.e. density). The basic model of this theory is formalized by the following equation (2) [20]:

$$P_c = VF_m \cdot P_m + (1 - VF_m) \cdot P_f \qquad (2)$$

where VF is the volume fraction of the component matrix (m) of the material and P is the property to be identified, P_c is the property of the composite material, P_m and P_f are the known property of matrix and filler, respectively. In this work, the UC is conceived as a composite material made of two components: the dielectric resin and the air. Therefore, the ε_{r-eff} of the composite UC can be identified by means of the ID%, rearranging the previous formula in equation (3) to calculate the ε_{R-eff}:

$$\varepsilon_{r-eff} = ID \cdot \varepsilon_{Res} + (1 - ID) \qquad (3)$$

where ε_{Res} is the relative permittivity of the resin [12], equal to 2.7.

The estimates of the effective relative permittivity of the UCs are reported in table 8: the actual ε_{R-eff} values are in the range of 1.36-2.27, which results in $\Delta\varepsilon_{R-eff}^A = 0.91$. Nonetheless, nominal and actual ε_{R-eff} values are still very close.
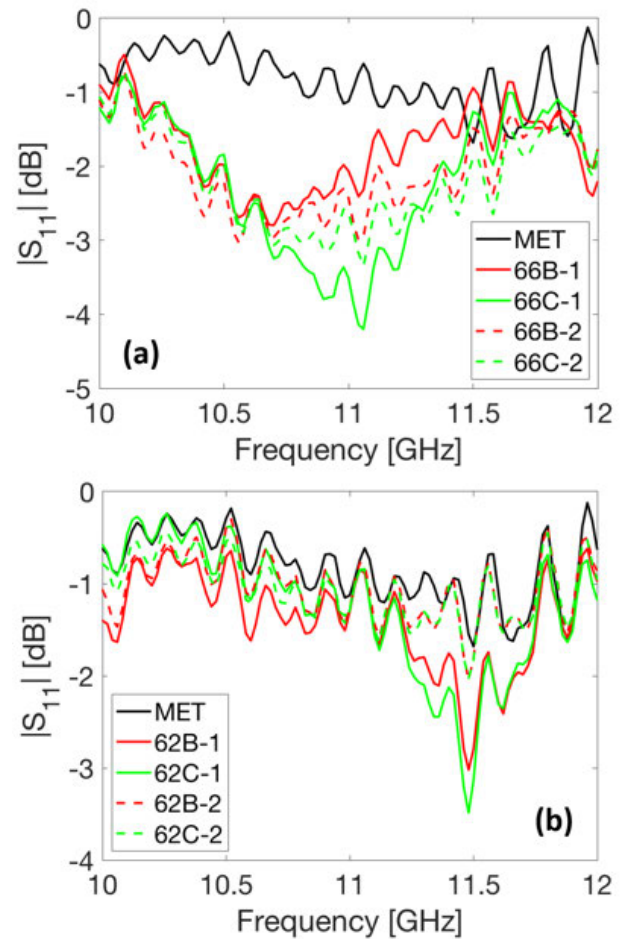

FIGURE 14. Scattering Parameter S_{11} for (a) samples 66B-1, 66B-2, 66C-1 and 66C-2 and b) samples 62B-1, 62B-2, 62C-1 and 62C-2. The black line refers to the aluminum plate (MET) used as reference.

V. SCATTERING PARAMETER S_{11} AND REFLECTED PHASE MEASUREMENTS

In order to measure the Scattering parameter S_{11} and the reflected phase in the X band (10-12 GHz), the prototypes of the 62 and 66 series were inserted into a standard X-band (WR-90) waveguide, connected to a Vector Network Analyser (VNA - Agilent Technologies, N9917A) by means of a SMA/waveguide adaptor. The plots of the scattering parameters S_{11}, reported in figure 14a-b, show good repeatability for all the tested prototypes: negative values and oscillating behavior of S_{11}, displayed also by the metal shorting plate, are reasonably due to the SMA-WG transition, which caused losses induced by non-perfect matching.

Figure 15 reports the experimental results of the reflected phase in the X band range, 10-12 GHz. In line with the previous results, very good repeatability of the phase curves can be observed. Similarly to the observations reported for the numerical results (figure 3a), the inspection of figures 15a-b confirms that larger phase shift is accomplished when passing from air-channel to bulk configurations, and so applying the maximum available ID% variation. This is particularly evident for prototypes 66B and 66C (figure 15a), where an
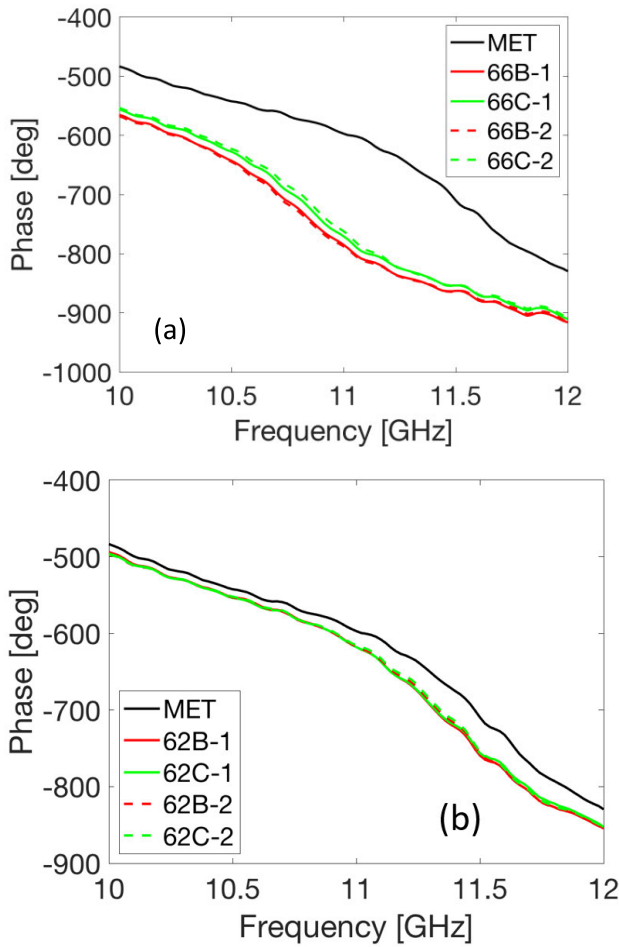
FIGURE 15. Phase curves for (a) samples 66B-1, 66B-2, 66C-1 and 66C-2, b) samples 62B-1, 62B-2, 62C-1 and 62C-2. The black line refers to the aluminum plate (MET) used as reference.

FIGURE 16. (a) Scattering Parameter S_{11} and (b) Phase curves for samples 42B, 42C, 44B and 44C. The black line refers to the aluminum plate (MET) used as reference.

average phase variation of about 25 degrees can be obtained throughout the range as the ID% varies from 74.29% to 53.96% (delta_ID% = 20.33 %). Conversely, for prototypes referring to 62B and 62C (figure 15b) the phase shift is about 5 degrees, achieved with an ID% variation equal to 6.78%. Consistently, all curves fall under the reference black line related to the metal plate. Nonetheless, ripples in both amplitude and phase measurements are evident and due to the not perfect match of the SMA-WG adaptor; this, in turn, modulates the phase difference between the curves in the range of interest.

The Scattering parameter S_{11} and the reflected phase in the mmwave range (20-40 GHz) related to 42B, 42C, 44B and 44C prototypes were plotted in figure 16. Also in this case, the measurements were carried out by inserting the samples in the WR28 waveguide connected to the VNA via a 2.4mm-connector to a WR28 waveguide adaptor, and exciting the fundamental mode TE_{10}. The Scattering parameter S_{11} (figure 16a) exhibits some dips, similarly to what observed also for X band measurements: the cause of such behavior can be imputed to the SMA-WG adaptor. Nonetheless, the trend of the curves is coherent with the change of the
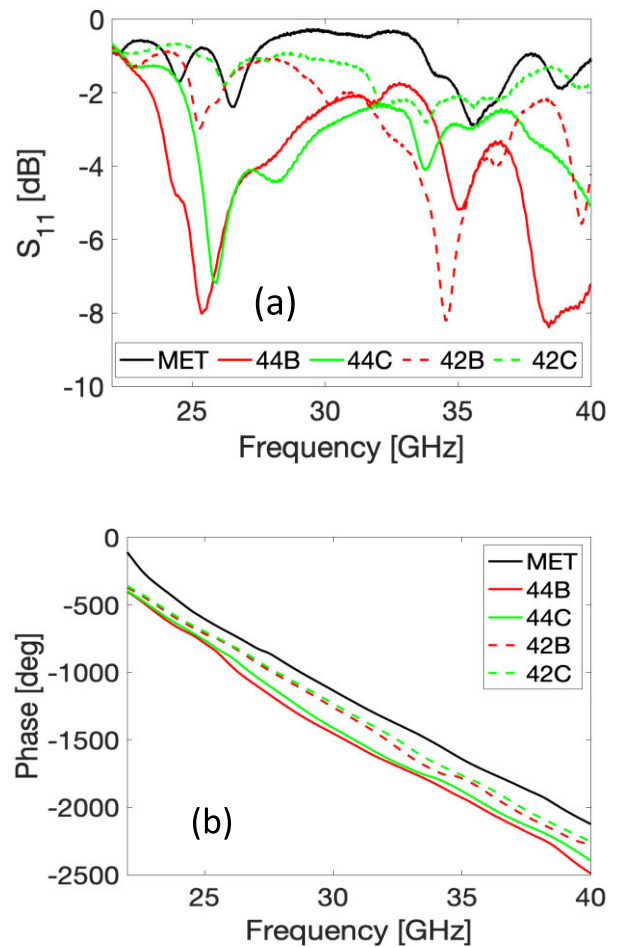
ID% of the structures: indeed, a frequency shift toward higher frequencies is observed as the ID% decreases. Figure 16b shows the measured reflected phase in the range between 26-40 GHz: the average phase variation measured comparing bulk and channeled samples 44B-44C (solid red and green lines) is about 43 degrees, obtained with a delta_ID% = 30.41%, while the comparison between 42B-42C (dashed red and green lines) provides a phase variation of 31 degrees achieved by a delta_ID% = 15.2%. Therefore, the phase shift between bulk and channeled configurations are in agreement with the numerical results, reported Figure 3b, although averagely smaller: indeed, 2.68 deg/air-channel are obtained for 44B-44C and 3.87 deg/air-channel for 42B-42C. Finally, the average phase variation exhibited between 44C and 42C is about 121 deg/8 channels, obtained by considering a delta_ID% = 19.74%.

VI. CONCLUSION
In this work, the design, fabrication and characterization of unit cells with micro channels aimed at phase control in 5G-mmwave applications were reported. The unit cells were designed to allow the control of the reflected phase:

this goal was obtained by tuning the unit cell size and the infill density percentage (ID%), and so, the effective relative permittivity of the structures. The ID% was engineered through the introduction of a number of uniformly distributed air micro-channels within the basic unit cell. Array configurations of unit cells having different sizes and ID% values were numerically analyzed via FEM analysis; the numerical results showed that very small phase variation over a wide band can be obtained especially in the mmwave range, depending on the air-channel number. The unit cell arrays, with and without micro-channels, were 3D printed by micro-inverted Stereolithography and resin polymer as material. This AM technology was feasible to fulfil the requirements of dimensional accuracy imposed by the unit cell and micro-feature sizes. Visual inspection of the prototypes highlighted that the most significant technological challenge was related to the fabrication of high aspect ratio micro-channels along the unit cell height. The geometrical analysis also put in evidence differences between nominal and actual sizes of micro-channels, which induced an increase of the actual ID% values and consequent increase of the effective relative permittivity of the prototypes. Finally, experimental results were performed in the two frequency ranges: the X band range, where scattering parameter S_{11} and reflected phase curves were measured by means of WR90 waveguide and a VNA; the mmwave range, where reflected phase variation measurements were obtained by means of a WR28 waveguide, a WG to coaxial transition and the VNA. The comparison between experimental and numerical analyses showed good agreement, especially in relation to the phase control and wideband behavior of the fabricated unit cell arrays. As micro-air channels may be filled with other materials, such as liquid crystals, these unit cells would allow to obtain wideband, tunable and smart surfaces, as well.

ACKNOWLEDGMENT

REFERENCES

[1] M. Xiao, S. Mumtaz, Y. Huang, L. Dai, Y. Li, M. Matthaiou, G. K. Karagiannidis, E. Bjornson, K. Yang, I. Chih-Lin, and A. Ghosh, "Millimeter wave for future mobile networks," *IEEE J. Sel. Areas Commun.*, vol. 35, no. 9, pp. 1909–1935, Sep. 2017.

[2] Q. Qiang, B. Huang, and M. Cao, "High power metamaterial based dielectric reflectarray antenna," in *Proc. 12th Int. Symp. Antennas, Propag. EM Theory (ISAPE)*, Dec. 2018, pp. 1–4, doi: 10.1109/ISAPE.2018.8634182.

[3] P. Nayeri, M. Liang, R. A. Sabory-Garcia, M. Tuo, F. Yang, M. Gehm, H. Xin, and A. Z. Elsherbeni, "3D printed dielectric reflectarrays: Low-cost high-gain antennas at sub-millimeter waves," *IEEE Trans. Antennas Propag.*, vol. 62, no. 4, pp. 2000–2008, Apr. 2014.

[4] S. Zhang, "Three-dimensional printed millimetre wave dielectric resonator reflectarray," *IET Microw., Antennas Propag.*, vol. 11, no. 14, pp. 2005–2009, Nov. 2017.

[5] A. Massaccesi, P. Pirinoli, V. Bertana, G. Scordo, S. L. Marasso, M. Cocuzza, and G. Dassano, "3D-printable dielectric transmitarray with enhanced bandwidth at millimeter-waves," *IEEE Access*, vol. 6, pp. 46407–46418, 2018, doi: 10.1109/access.2018.2865353.

[6] S. Zhang, D. Cadman, J. C. Vardaxoglou, R. Mittra, and W. Whittow, "Enabling additive manufacturing for microwave and mm-wave components fabrication," in *Proc. Int. Conf. Microw. Millim. Wave Technol. (ICMMT)*, May 2019, pp. 1–3, doi: 10.1109/ICMMT45702.2019.8992908.

[7] S. Zhang, R. K. Arya, S. Pandey, Y. Vardaxoglou, W. Whittow, and R. Mittra, "3D-printed planar graded index lenses," *IET Microw., Antennas Propag.*, vol. 10, no. 13, pp. 1411–1419, Oct. 2016, doi: 10.1049/iet-map.2016.0013.

[8] B. T. Malik, V. Doychinov, S. A. R. Zaidi, I. D. Robertson, and N. Somjit, "Antenna gain enhancement by using low-infill 3D-printed dielectric lens antennas," *IEEE Access*, vol. 7, pp. 102467–102476, 2019, doi: 10.1109/access.2019.2931772.

[9] *COMSOL Multiphysics v.5.4*, COMSOL AB, Stockholm, Sweden, 2018. [Online]. Available: www.comsol.com

[10] P. Kumar, S. Dwari, and J. Kumar, "Design of biodegradable quadruple-shaped DRA for WLAN/Wi-max applications," *J. Microw., Optoelectron. Electromagn. Appl.*, vol. 16, no. 3, pp. 867–880, Sep. 2017.

[11] V. Marrocco, V. Basile, I. Fassi, M. Grande, D. Laneve, F. Prudenzano, and A. D'Orazio, "Dielectric resonant antennas via additive manufacturing for 5G communications," in *Proc. Photon. Electromagn. Res. Symp. Spring (PIERS-Spring)*, Jun. 2019, pp. 17–20.

[12] V. Basile, M. Grande, V. Marrocco, D. Laneve, S. Petrignani, F. Prudenzano, and I. Fassi, "Design and manufacturing of super-shaped dielectric resonator antennas for 5G applications using stereolithography," *IEEE Access*, vol. 8, pp. 82929–82937, 2020, doi: 10.1109/ACCESS.2020.2991358.

[13] K. V. Wong and A. Hernandez, "A review of additive manufacturing," *ISRN Mech. Eng.*, vol. 2012, pp. 1–10, Jan. 2012.

[14] V. Basile, F. Modica, and I. Fassi, "Analysis and modeling of defects in unsupported overhanging features in micro-stereolithography," in *Proc. 21st Design Manuf. Life Cycle Conf., 10th Int. Conf. Micro- Nanosyst.*, vol. 4, Aug. 2016, Art. no. V004T08A020, doi: 10.1115/DETC2016-60092.

[15] F. Modica, V. Basile, S. Ruggeri, G. Fontana, and I. Fassi, "Can a low cost sensing system be exploited for high precision machining?" *Procedia CIRP*, vol. 75, pp. 391–396, Jan. 2018.

[16] V. Basile, F. Modica, G. Fontana, S. Ruggeri, and I. Fassi, "Improvements in accuracy of fused deposition modeling via integration of low-cost on-board vision systems," *J. Micro Nano-Manuf.*, vol. 8, no. 1, Mar. 2020, Art. no. 010905, doi: 10.1115/1.4046038.

[17] T. J. Collins, "ImageJ for microscopy," *BioTechniques*, vol. 43, no. 1S, pp. S25–S30, Jul. 2007.

[18] M. C. Bustos, F. Concha, R. Bürger, and E. M. Tory, "Theory of mixtures," in *Sedimentation and Thickening. Mathematical Modelling (Theory and Applications)*, vol. 8. Dordrecht, The Netherlands: Springer, 1999, doi: 10.1007/978-94-015-9327-4_2.

[19] S. Ahmed and F. R. Jones, "A review of particulate reinforcement theories for polymer composites," *J. Mater. Sci.*, vol. 25, no. 12, pp. 4933–4942, Dec. 1990, doi: 10.1007/BF00580110.

[20] M. Alger, *Polymer Science Dictionary*, 3rd ed. Springer, 2017, doi: 10.1007/978-94-024-0893-5.

VITO BASILE received the M.Sc. degree in engineering of management from the University of Calabria, Italy, in 1998, and the master's degree in industrial research from the National Research Council, Italy, in 2003. From 1999 to 2002, he was an Assistant Professor of mechanical technologies and production systems with University of Calabria. He gained a relevant industrial experience as a Mechanical Designer, a Technical Manager, and a Research and Development Project Manager. He has coauthored several international patents. In 2012, he joined CNR-ITIA (currently CNR-STIIMA), as a Researcher. His current research interests include production systems, automation, robotics and manufacturing, additive manufacturing technologies, nano-structured materials, and micro-manufacturing technologies. He received the IF Award 2012.

VALERIA MARROCCO received the M.Sc. and Ph.D. degrees in electronic engineering from the Polytechnic University of Bari, in 2003 and 2007, respectively. Since 2007, she has been a Researcher with the Polytechnic University of Bari, where she was involved in the design of photonics, plasmonics, and nano-technology-based devices. She was a Lecturer Assistant and a Students' Supervisor. Since 2011, she has been with CNR-ITIA (currently CNR-STIIMA), where she is currently a part of the Research Group MEDIS. She is involved in research activities concerning micro-manufacturing of micro-components and devices, related to micro-EDM, and, in particular, to the development of monitoring system and modeling techniques. She has coauthored several peer-reviewed articles and also participated as an invited speaker to several international conferences. Her research interest includes micro-additive manufacturing for the design and development of 5G and mmwave components. She is also a referee for scientific international journals (ISI-WoS) and took part to different national projects.

MANUELA SPINA received the B.Sc. degree in electronic and telecommunication engineering and the M.Sc. degree *(summa cum laude)* in telecommunication engineering from the Polytechnic University of Bari, Italy, in 2017 and 2020, respectively. Since 2020, she has been working with SM-OPTICS (part of SIAE Microelettronica Group) Company, Bari. Her main scientific interests include 5G communication, smart antennas, and optical networks.

IRENE FASSI received the Ph.D. degree in industrial technologies and the M.Sc. degree in mechanical engineering from the Politecnico di Milano, in 2001and 1997, respectively. Since 1998, she has been a full-time Researcher with CNR-ITIA (now CNR-STIIMA), where she founded and leads the Research Group MEDIS. She is currently an Adjunct Professor in robotics, precision engineering, and advanced manufacturing systems with the University of Brescia and the Politecnico di Milano. She is a member of the Executive Board of SIRI (Italian Robotics and Automation Association), AITeM (Italian Association of Manufacturing Technologies), and the ASME/DED Technical Committee on Micro and Nano Manufacturing. She is also serves as a President elect for the International Institution for MicroManufacturing.

ANTONELLA D'ORAZIO (Member, IEEE) received the master's degree *(summa cum laude)* in electrical engineering, from the Polytechnic University of Bari, in 1983 and the Ph.D. degree in electromagnetisms from the Electronics and Electrotechniques Department DEI, Polytechnic University of Bari, in 1987. Since 1983, she joined the Electronics and Electrotechnics Department DEE (now Department of Electrical and Information Engineering DEI), Polytechnic University of Bari, where she was an Assistant Professor in 1990 and an Associate Professor in 1998. Since 2003, she has been a Full Professor of electromagnetic fields. Her research interests include the analysis and propagation in linear and nonlinear integrated optic devices, the design, fabrication and characterization of microwave devices and antennas, photonic crystal devices, metamaterials, plasmonic structures, and graphene based devices. She has coauthored over 320 publications on journals and international conferences, lectures and invited papers. She is a member of IEEE, OSA, AEIT Italy, S.I.EM, and SIOF (Italian Branch of the European Optical Society).

MARCO GRANDE received the master's degree *(summa cum laude)* in electronic engineering and the Ph.D. degree from the Polytechnic University of Bari, 2006 and 2010, respectively. Since October 2015, he has been an Assistant Professor in electromagnetic fields with the Polytechnic University of Bari. He is involved in several national and international research projects (US Army and H2020). He has coauthored about 100 publications on international journals and conference proceedings and one patent. He is a member of the Editorial Board of *Scientific Reports* (Nature-Springer) and serves as a reviewer for several journals. His research interests include photonic crystals, plasmonic nanostructures, optical and microwave graphene-based devices, and smart antennas.

• • •